Journal of Solid State Chemistry **146,** 464–472 (1999)
Article ID jssc.1999.8394, available online at http://www.idealibrary.com on IDEAL®

Color of Mn(V)-Substituted Apatites $A_{10}((B, Mn)O_4)_6F_2$, A = Ba, Sr, Ca; B = P, V

K. Dardenne,* D. Vivien,*,[1] and D. Huguenin†

*Laboratoire de Chimie Appliquée de l'Etat Solide, UMR CNRS n°7574, ENSCP, 11 rue Pierre et Marie Curie, 75231 Paris Cedex 05, France; and †Centre de Recherches RHODIA, 52 rue de la Haie Coq, 93308 Aubervilliers, France

Received January 8, 1999; in revised form May 14, 1999; accepted May 24, 1999

The relationship between color and chemical composition in a series of Mn(V)-substituted fluoroapatites $A_{10}(B_{1-x}Mn_xO_4)_6F_2$ is studied as a function of the nature of A = Ca, Sr, Ba; B = P, V, and the Mn substitution, x. These apatites exhibit deep blue to green colors. Saturation effects occur for some tetrahedral Mn(V) absorption bands, which are correlated to the large cross section of the corresponding transitions. These account for the blue to green color change with increasing the Mn content, x. The crystal field experienced by the Mn(V) ion is independent of x and of the nature of the B ion it replaces. This is because Mn(V) imposes its own size to the host lattice (mean Mn–O distance = 1.72 Å in all cases). The displacement of the Mn(V) absorption bands for A over the series Ca, Sr, to Ba is mainly due to an increasing Mn–O bond covalency. © 1999 Academic Press

1. INTRODUCTION

Oxide matrices doped with tetrahedral d^2 transition-metal ions, such as Cr(IV), Mn(V), and Fe(VI), exhibit bright colors due to the large absorption cross sections (1, 2). The luminescence properties of these ions are also remarkable. While Mn(V) and Fe(VI) show a sharp line luminescence in the near IR (3–7), the Cr (IV) doped compounds give rise to a broadband luminescence, allowing applications as tunable laser in the near IR region (8, 9).

The $(MnO_4)^{3-}$ ions substitute isovalent tetrahedral anions such as $(PO_4)^{3-}$ or $(VO_4)^{3-}$ without any problems of charge compensation, leading to phosphates and vanadates, which exhibit saturated colors ranging from blue to green. This could lead to their application as inorganic pigments (1, 10, 19). The optical properties of several Mn(V)-doped phosphates or vanadates, such as $Sr_{10}(PO_4)_6Cl_2$ (5, 11, 12), $Ba_{10}(PO_4)_6Cl_2$ (1, 2, 4, 13), $Ca_2(VO_4)Cl$ (1, 4, 13, 14), Li_3PO_4 (4, 15) …, have already been studied, for the most part using fluorescence spectroscopy and will serve here as references for the assignment of the Mn(V) optical transitions.

The aim of the present work is to study the influence of the chemical composition of a series of Mn(V)-substituted apatites $A_{10}(BO_4)_6F_2$ (A = Ca, Sr, Ba and B = V, P) on their color. Particular emphasis will be laid on the influence of the substitution x, as well as the effect of the nature of the A (Ca, Sr, Ba) and B (P, V) cations.

2. SYNTHESIS AND CHARACTERIZATION OF Mn(V) DOPED FLUOROAPATITES

The fluoroapatite powders $A_{10}(B_{1-x}Mn_xO_4)_6F_2$ (A = Ca, Sr, Ba and B = V, P) were prepared (16, 17) by heating a mixture of alkaline-earth carbonate ACO_3, manganese (III) oxide Mn_2O_3, ammonium fluoride, and ammonium dihydrogenophosphate or vanadium oxide V_2O_5, in appropriate amounts. The precursors were intimately mixed by grinding them together, then pressed into pellets and repeatedly heated for 12 h until a pure phase was obtained under the following conditions:

— The low manganese-substituted phosphates ($x \leq 0.3$) were tempered in air at 1250°C.

— The remaining manganese-substituted phosphates ($x > 0.3$) and substituted vanadates were heated at 1000°C in an oxygen stream.

Compounds corresponding to the following nominal compositions were synthesized:

— $Ba_{10}(P_{1-x}Mn_xO_4)_6F_2$: x = 0; 0.001; 0.01; 0.02; 0.033; 0.05; 0.1; 0.2; 0.3; 0.5; 0.6; 0.8; and 1,

— $Ba_{10}(V_{1-x}Mn_xO_4)_6F_2$: x = 0; 0.02; 0.2; 0.6; 1

— $Sr_{10}(P_{1-x}Mn_xO_4)_6F_2$: x = 0.01; 0.1; 0.2; 0.3

— $Ca_{10}(P_{0.99}Mn_{0.01}O_4)_6F_2$

— $A_{10}(V_{0.98}M_{0.02}O_4)_6F_2$ (A = Sr, Ca).

The X-ray diffraction powder pattern confirms that, to the sensitivity of the technique, a single phase with apatite structure is obtained. Only the strontium phosphate apatites with x = 0.2 and 0.3 Mn exhibited some additional peaks in their X-ray diffraction diagram.

[1] To whom correspondence should be addressed.

0022-4596/99 $30.00

Chemical analysis was performed at the "laboratoire central d'analyses du CNRS de Vernaison" (France) on the manganese-doped apatites after dissolution in perchloric acid. The fluorine content was determined using a F^- specific electrode and cation content through inductively coupled plasma–atomic emission spectroscopy (ICP–AES). No significant differences between the experimental and theoretical Mn-substituted apatites formula are observed, except for the fluorine content, which is as low as 50% of the expected value for the less Mn(V)-substituted compounds. This fluorine loss is compensated by oxygen ions ($2F^- \leftrightarrow O^{2-}$). Therefore, the studied compounds are in fact oxo-fluoroapatites instead of fluoroapatite. However, since the shortest P(Mn)–F distance of around 4 Å (18) is much longer than ~ 1.7 Å for the Mn–O distances in $(MnO_4)^{3-}$ tetrahedra (19), this partial $F^- \leftrightarrow O^{2-}$ substitution will not significantly effect the Mn(V) optical properties reported below. Theoretical formulas are used below to identify the various compounds.

3. X-RAY DIFFRACTION STUDY

Fluoroapatite crystallizes with an hexagonal structure, space group $P6_3/m$, with one formula unit per unit cell (18). In $A_{10}(BO_4)_6F_2$, the 10 A^{2+} ions are distributed over two different crystallographic sites: four of them lie in a nine-coordinated oxygen polyhedra, and the six remaining ions are sevenfold coordinated, with six oxygen and one fluoride ions. There is only one kind of B(V) ion, which lies in tetrahedral sites. B shares its oxygen coordination polyhedron with A cations, but not with the other B ions.

The true symmetry of $(BO_4)^{3-}$ anions (B = P, V, Mn) in apatites is lower than T_d although the four B–O distances are very similar. For example, P–O distances in $Ba_{10}(PO_4)_6F_2$ (18) are 1.548 Å, 1.539 Å and 2×1.536 Å. The actual symmetry is C_s (approximately C_{3v}).

X-ray diffraction patterns are recorded using a SIEMENS D5000 Diffractometer (Co$K\alpha$ radiation). The lattice constants of the various compounds synthesized are given Table 1 and Table 2. Most constants are computed using the U-Fit software (20). For the compounds $Ba_{10}(PO_4)_6F_2$ and $Ba_{10}(MnO_4)_6F_2$, whose structures were refined using the Rietveld method (21), the lattice parameters are determined using the FULLPROF software (22).

Values of the unit-cell parameters of the compounds with $x = 0$ or 1 can be compared with the literature data. There is a good agreement between our results and those reported for $Ba_{10}(PO_4)_6F_2$ single crystals by Mathew *et al.* (18) and by Lavat *et al.* for powder data (23). The data given in Table 1 for the strontium fluorophosphate ($Sr_{10}(P_{1-x}Mn_xO_4)_6F_2$) and barium vanadate ($Ba_{10}(V_{1-x}Mn_xO_4)_6F_2$) apatite are similar to those obtained by Grisafe *et al.* (17).

In contrast our unit-cell parameters for $Ba_{10}(PO_4)_6F_2$ and $Ba_{10}(MnO_4)_6F_2$ are significantly different from those reported by Grisafe *et al.* ($a = 10.220$ Å, $c = 7.665$ Å) (2) and by Manca *et al.* ($a = 10.380$ Å, $c = 7.730$ Å) (24), respectively. This may be due to a different stoichiometry of the compounds studied by these authors than that of our

TABLE 1
Lattice Constants for the Low Mn(V) Substituted Apatites

Compounds	Lattice constants (Å) versus x value						
	0	0.001	0.01	0.02	0.033	0.05	0.10
$Ca_{10}(P_{1-x}Mn_xO_4)_6F_2$		9.376 6.885	9.384 6.887	9.377 6.885			
$Sr_{10}(P_{1-x}Mn_xO_4)_6F_2$	9.716 7.283	9.719 7.287	9.733 7.290	9.731 7.294		9.722 7.289	9.736 7.301
$Ba_{10}(P_{1-x}Mn_xO_4)_6F_2$	10.1521 7.7118	10.155 7.720	10.152 7.712	10.150 7.712	10.172 7.733	10.163 7.720	10.176 7.726
$Ca_{10}(V_{1-x}Mn_xO_4)_6F_2$				9.70 7.00			
$Sr_{10}(V_{1-x}Mn_xO_4)_6F_2$				10.02 7.44			
$Ba_{10}(V_{1-x}Mn_xO_4)_6F_2$	10.419 7.845			10.39 7.81			

Note. Parameter a is above, parameter c below. Gray boxes correspond to compounds that do not exist or were not synthesized. Errors are at much 1 unit of the significant digit given. The $Ba_{10}(PO_4)_6F_2$ unit cell parameters were determined with greater acuracy through a Rietveld structural refinement (32).

TABLE 2
Lattice Constants for the High Mn(V)-Substituted Apatites

Compounds	Lattice constants (Å) versus x value					
	0.20	0.30	0.50	0.60	0.80	1
$Sr_{10}(P_{1-x}Mn_xO_4)_6F_2$	*9.747* *7.307*	*9.746* *7.308*				
$Ba_{10}(P_{1-x}Mn_xO_4)_6F_2$	10.194 7.738	10.211 7.740	10.247 7.784	10.250 7.802	10.300 7.825	10.3437 7.8639
$Ba_{10}(V_{1-x}Mn_xO_4)_6F_2$	10.396 7.844			10.368 7.851		

Note. Parameter *a* is above, parameter *c* below. The values in italics correspond to compounds having additional lines in their X-ray diffraction pattern. Gray boxes correspond to compounds that do not exist or were not synthesized. Errors are at much 1 unit of the significant digit given. The $Ba_{10}(MnO_4)_6F_2$ unit cell parameters were determined with greater accuracy through a Rietveld structural refinement (32).

samples, whose compositions were checked through chemical analysis.

The upper Mn(V)-substitution limit depends on the nature of the alkaline-earth. For barium apatite, a solid solution exists for the entire range of compositions between $Ba_{10}(BO_4)_6F_2$ and $Ba_{10}(MnO_4)_6F_2$; for strontium or calcium phosphate apatite the range is much smaller. The limit of substitution was determined by the appearance of additional lines in the X-ray diffraction patterns and by the invariance of the lattice constants. In the case of phosphate apatite, substitution of up to 3% for $A = Ca$ and 50% for $A = Sr$ are reported (1). Our results show substitution limits significantly smaller: $\sim 2\%$ for Ca and $\sim 20\%$ for Sr.

Figures 1 and 2 depict lattice constants of the barium apatite phases as a function of manganese content. In the case of barium phosphate apatite, the lattice constants increase with increasing manganese content. This is expected since the Mn(V) radius (0.33 Å) is larger than that of phosphorus (0.17 Å) (25) (Fig. 1). This confirms that Mn(V) enters the apatite lattice instead of forming a second phase, which may be undetectable on the X-ray diffraction patterns, especially at low manganese levels. The variation is slightly more complicated for the vanadate apatite (Fig. 2), since the lattice parameter *a* decreases while *c* increases when the manganese content increases. The small unit-cell variation (-1.2%) between barium vanadate and manganate apatites reflects the similarity between the V(V) (0.35 Å) and Mn(V) (0.33 Å) radii (25).

In both case, it must be pointed out that the lattice parameters obey the Vegard's law (linear dependence upon

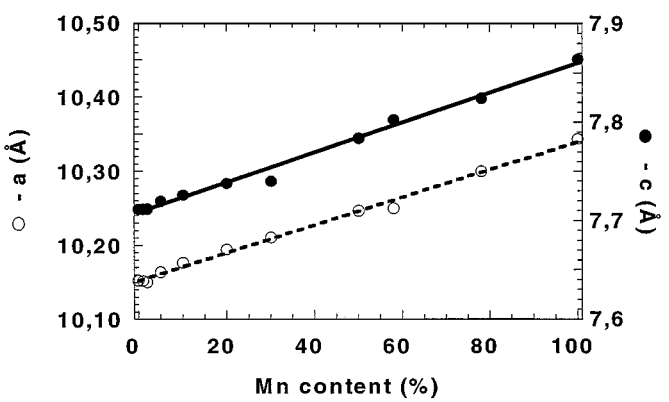

FIG. 1. Variation of lattice constants a (empty circles) and c (filled circles) with the percent manganese introduced in the apatite $Ba_{10}(P_{1-x}Mn_xO_4)_6F_2$.

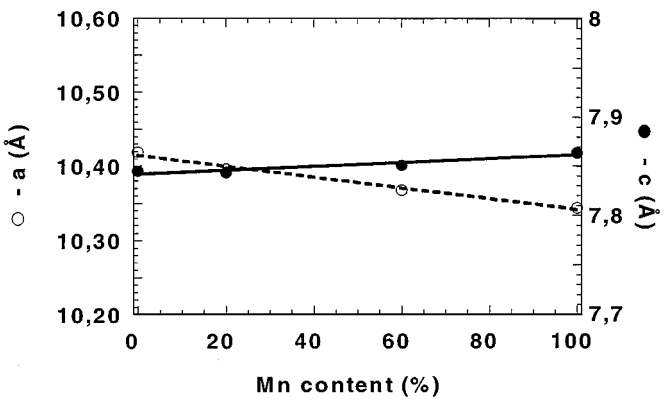

FIG. 2. Variation of lattice constants a (empty circles) and c (filled circles) with the percent manganese introduced in the apatite $Ba_{10}(V_{1-x}Mn_xO_4)_6F_2$.

the manganese content). Usually, departure from the Vegard's law in solid solutions indicates clustering of the dopant (26). This is not the case here and therefore Mn(V) ions are probably randomly distributed over the phosphorus or vanadium sublattice.

4. DIFFUSE REFLECTANCE SPECTROSCOPY

These measurements were carried out to characterize compounds coloration. The absorption spectrum of Mn(V) in barium fluoroapatite has not been reported in the literature. However spectra for related compounds such as barium chloroapatite (19) are known, which can be used as a reference.

Diffuse reflectance spectra were recorded on a VARIAN CARY 5 spectrometer equipped with an integrating sphere. The specular component of the reflectance has been rejected in order to scale the spectrum ordinate with the Kubelka–Munk function $F(R) = (1 - R)^2/2R = K/S$ (27), in which R is the diffuse reflectivity of the sample normalized to the PTFE reference at each wavelength, S the diffusion coefficient, and K the absorption coefficient. When conditions of complete specular component rejection, small powder grain size, and random orientation are fulfilled, the $F(R)$ function is closely related to the optical density of the sample (27), and the $F(R) = f(\lambda)$ spectrum has the appearance of an absorption spectrum.

Some absorption spectra were recorded at low temperature (30 K) on KBr pellets containing about 3% weight of apatites. Although the signal-to-noise ratio of these spectra was not very good, they had a resolution superior to the diffuse reflectance spectra. The low-temperature absorption spectra are very useful in determining the position of the shoulders on the absorption bands.

We will describe an example of these spectra in details and compare the observed transitions with the expected transitions, then we will discuss the effects of the manganese ratio, nature of the alkaline-earth ion, and size of the B site on the coloration.

4.1. Absorption Spectra and Selection Rules

The energy states for a Mn(V) (d^2 electronic configuration) in a tetrahedral crystal field discussed in several papers (12, 28–31) are presented Fig. 3. Assuming a regular tetrahedral environment (T_d), five d–d transitions are expected in the 250 to 1300-nm wavelength range. There are three spin-allowed transitions from the ground state $^3A_2$ to $^3T_2$, $^3T_1(^3F)$, and $^3T_1(^3P)$ states. The $^3A_2 \rightarrow {}^3T_2$ transition is symmetry forbidden and the $^3A_2 \rightarrow {}^3T_1(^3P)$ corresponds to a two-electron jump (28). They are both expected to be weak. Therefore, only one strong absorption band in the visible range corresponding to the $^3A_2 \rightarrow {}^3T_1(^3F)$ transition will be observed.

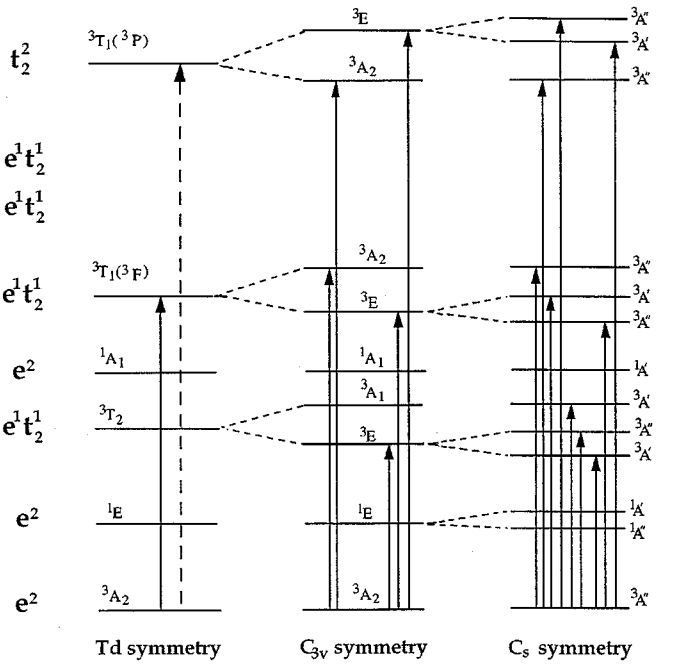

FIG. 3. Energy diagram for Mn(V) in a tetrahedral crystal field and effects of lowering the symmetry. The order of the states arising from the splitting of the T_d, E, and T states is arbitrary.

The lowering of symmetry to C_{3v} and C_s (Fig. 3) leads to a change of selection rules since the transition to the former $^3T_2$ state becomes symmetry allowed and to a splitting of states which were degenerated in regular tetrahedral symmetry. These modifications influence the color of the Mn(V)-doped apatites. It modifies the range of absorbed wavelength by either broadening of the $^3A_2 \rightarrow {}^3T_1(^3F)$ band and/or shifting some $^3T_2$ and $^3T_1(^3P)$ energy substates into the red and blue part of the visible spectrum, respectively, both leading to a modification of the coloration.

An example of a Mn(V)-substituted apatite diffuse reflectance spectrum is given in Fig. 4. This spectrum is transformed according to the Kubelka–Munk function, which should give an intensity scale proportional to the manganese content, assuming that the conditions given above are fulfilled. This figure exhibits the different bands associated with the $^3A_2 \rightarrow {}^3T$ transitions. They are assigned according to literature results on similar Mn(V)-doped compounds such as $Sr_{10}(PO_4)_6Cl_2$ (12), $Sr_{10}(VO_4)_6F_2$ (28), and $Ca_2(PO_4)Cl$ (29). As expected, the spectrum is dominated by the $^3A_2 \rightarrow {}^3T_1(^3F)$ transition localized in the visible range. This band has three components, confirming the C_s symmetry of the site occupied by Mn(V) in the apatite structure.

A very intense absorption band, corresponding to an oxygen ions to manganese orbitals charge transfer transition, is observed in the UV range around 315 nm. We will confirm its attribution later in this paper.

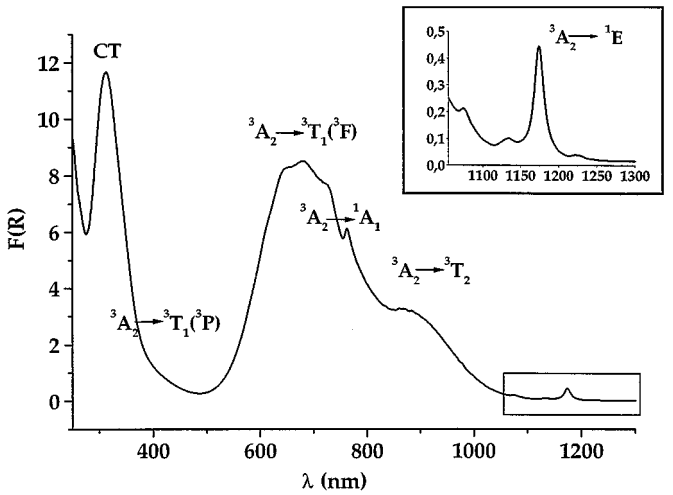

FIG. 4. Diffuse relectance spectrum of $Ba_{10}(P_{0.8}Mn_{0.2}O_4)_6F_2$ transformed according to the Kubelka–Munk function (CT: charge transfer transition).

TABLE 3
Position and Assignment of Absorption Bands for $Ba_{10}(P_{0.8}Mn_{0.2}O_4)_6F_2$ Apatite

Wavelength (nm)	Excited state involved
1174.2	^1E
~ 873	$^3T_2$
762.3	$^1A_1$
728	
701	$^3T_1(^3F)$
680	
644	(+ $^1A_1$ vibronic satellites?)
614	
587	
~ 405	$^3T_1(^3P)$
~ 315	Charge transfer

Note. Values corresponding to the diffuse reflectance spectra are given in bold numbers, remaining values are additional components observed on the absorption spectra at liquid He temperature.

The spin forbidden zero-phonon transitions between the ground state and the ^1E and $^1A_1$ singlet is observed in Fig. 4. Vibronic satellites accompaning the $^3A_2 \rightarrow {}^1E$ transition which arise from the coupling between the electronic states and three of the four vibration modes (ν_2, ν_3 and ν_4) of the $(MnO_4)^{3-}$ group (32), are seen in Fig. 4 insert.

Careful inspection of the Mn(V)-substituted apatite absorption spectrum obtained at liquid helium temperature on KBr pellets reveals that there are three additional shoulders on the $^3A_2 \rightarrow {}^3T_1(^3F)$ transition band. This is twice that expected, even for C_s site symmetry (Fig. 3). These additional features may arise from a second type of Mn(V) site belonging to a manganese-rich parasitic phase, which may occur in sufficienty small amounts to be undetected by X-ray diffraction. However, it seems more likely that the additional bands are vibronic satellites of the $^1A_1$ zero-phonon line, similar to those observed for the ^1E transition. The positions and assignments of the different absorption bands (12, 28, 29) are given in Table 3.

Minor amounts of manganese ions in other oxidation states, mainly II and VI should possibly occur in the Mn-doped apatites. The luminescence of Mn(II) in *A* sites of apatites is well documented (33). However, because of the spin-forbidden character of the Mn(II) absorption transitions, this ion will not significantly contribute to the diffuse reflection spectra investigated here. Mn(VI) ions were studied in several compounds in which it substitutes hexavalent ions like S, Se, Cr (34). Here, since it should replace *B*(V) ions, charge compensation will be needed. Mn(VI) presents only one *d–d* band (d^1 ion) located around 800 nm and several charge transfer transitions in the visible and UV range (34). It exhibits strong fluorescence with well-resolved vibronic fine structure (34). This was not observed in the compounds studied (32). However, further studies using for instance EPR (35), should be performed in order to rule out the presence of Mn(VI).

4.2. *Influence of the Manganese Content on the Coloration of Mn(V)-Doped Apatites*

We have studied the effect of the manganese content on the coloration of the Mn(V)-substituted apatites in the solid solution series $Ba_{10}(BO_4)_6F_2$ (B = P, V)–$Ba_{10}(MnO_4)_6F_2$.

These compounds show a very deep color which goes from turquoise-blue to dark green when the Mn(V) content increases. This color variation is depicted in Fig. 5 on a $L^*a^*b^*$ chromaticity diagram in which a is the green to red component and b the blue to yellow one (according to the sign of these coordinates). The L component describes

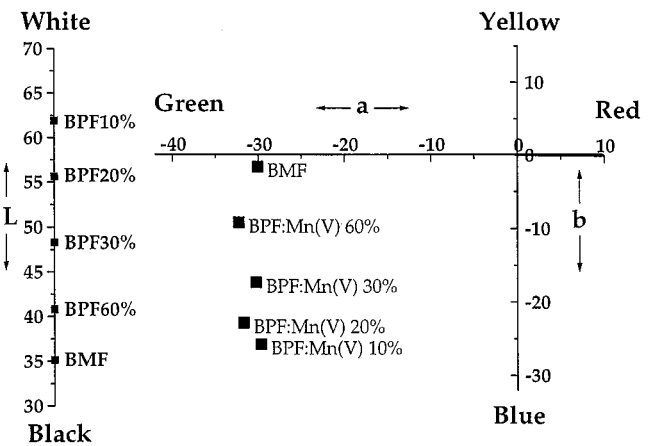

FIG. 5. $L^*a^*b^*$ chromaticity diagram showing the color coordinates of various compounds of $Ba_{10}(P_{1-x}Mn_xO_4)_6F_2$ (BPF: Mn x%) and of $Ba_{10}(MnO_4)_6F_2$ (BMF).

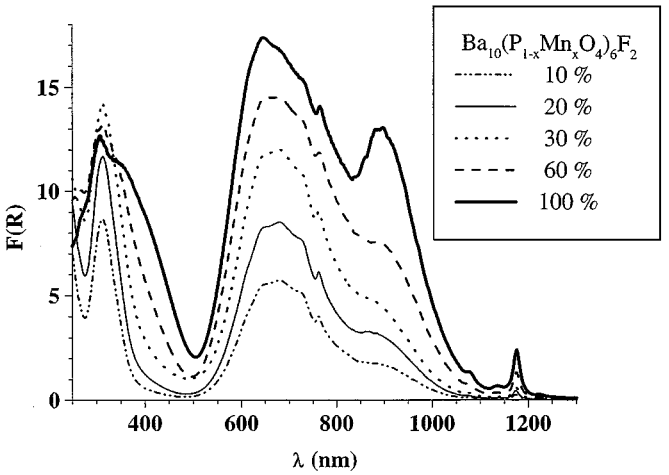

FIG. 6. Diffuse reflectance spectra of $Ba_{10}(P_{1-x}Mn_xO_4)_6F_2$ transformed according to the Kubelka–Munk function for various manganese contents.

the darkness of the color: $L = 0$ for black and 100 for white. The chromatic coordinates are calculated from the diffuse reflectance spectra of several members of the $Ba_{10}(PO_4)_6F_2$ – $Ba_{10}(MnO_4)_6F_2$ solid solution using the COLOR software from VARIAN. Figure 5 indicates that the color change from blue to green comes mainly from a reduction of the blue coordinate when the manganese content increases. Since the lattice constants increase linearly with the Mn(V) content (see Section 3), this color change could arise from a shift of the reflection bands toward longer wavelengths. This means a decrease of the crystal field strength. This is, however, incorrect, as shown in Fig. 6, which presents several diffuse reflectance spectra transformed according to the Kubelka–Munk function. Notice that there is no displacement of the absorption bands, indicating that there is no variation of the crystal field strength with the manganese content. Nevertheless, the contribution of the absorption bands corresponding to the $^3A_2 \rightarrow {}^3T_1(^3P)$ and $^3A_2 \rightarrow {}^3T_2$ transitions to the reflectance spectra increases compared to the contribution of the $^3A_2 \rightarrow {}^3T_1(^3F)$ transition when the Mn(V) content increases. This induces a modification of the shape of the diffuse reflectance spectra. The change of the relative absorption intensities near 450 nm is responsible for the color shift from blue to green.

We have studied the evolution of F(R) versus the Mn(V) concentration for some particular wavelengths, representative of the different transitions involved in the spectra. The curves $F(R) = f(x)$ are plotted in Fig. 7. Two kinds of behavior are observed:

— A linear variation of F(R) versus the manganese content, x, predicted by the Beer–Lambert Law. This confirms that F(R) is proportional to the absorption coefficient. Such a behavior occurs for the absorption bands associated with the transition to the $^3T_1(^3P)$, $^3T_2$, and ^1E states. These transitions have weak absorption cross sections, σ, since the former corresponds to a two-electron jump (in strong crystal-field approximation), while the two other are symmetry and spin forbidden, respectively.

— A saturation of F(R) for x values greater than ~ 0.30. This is observed for the transition to the $^3T_1(^3F)$ state and for the charge transfer transitions, all having large absorption cross sections.

These two kinds of behavior demonstrate that the color change is due to a selective saturation phenomenon. To account for this saturation effect and determine the factors which could influence it, we used a simple three-energy state model depicted in Fig. 8.

The number *1* is the $^3A_2$ Mn(V) ground state. The ^1E emitting state is labeled *3* and the states marked *2* are those responsible for the absorption (i.e., $^3T_2$, $^3T_1(^3F)$, and $^3T_1(^3P)$). We consider that the energy of the incident photon flux corresponds to the *1* to *2* transitions and that nonradiative relaxations from *2* to *3* are very efficient so that only *3* is populated and gives rise to spontaneous emission.

One can describe the absorption from *1* and spontaneous emission from *3* with the Einstein equations [1] and [2], respectively

$$\frac{dN_R}{dt} = -N_R\sigma\phi \qquad [1]$$

$$\frac{d(N_T - N_R)}{dt} = -\frac{(N_T - N_R)}{\tau}, \qquad [2]$$

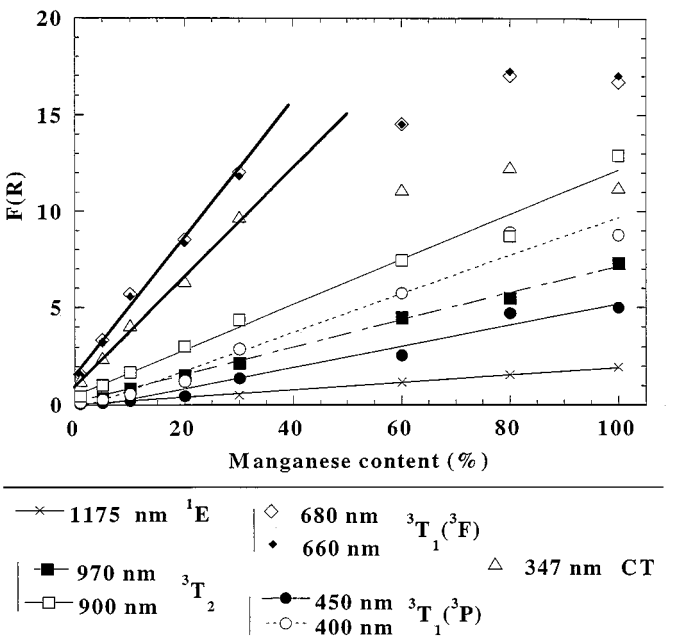

FIG. 7. Variation of F(R) with the manganese content, x, for several selected wavelengths associated with different optical transitions in $Ba_{10}(P_{1-x}Mn_xO_4)_6F_2$ (CT = charge transfer transition).

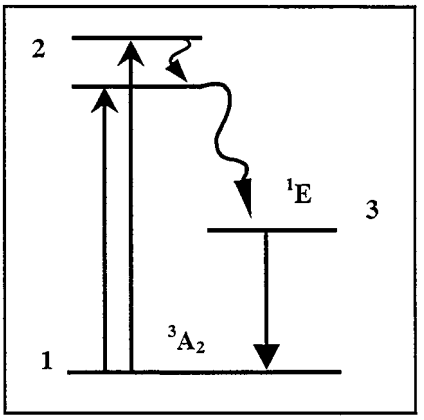

FIG. 8. Three-level energy scheme to explain the saturation of some Mn(V) absorption transitions.

where N_R is the population of the ground state, N_T is the total number of Mn(V), σ the *1–2* absorption cross section, τ the radiative lifetime of *3* and ϕ the photon flux (photons/cm^{2}s).

Considering the attenuation of the light beam in a medium of length x with an absorption coefficient $\alpha_{max} = \sigma N_T$, we have $\phi = \phi_0 \exp(-\sigma N_R x)$. Using these relations and combining Eqs. [1] and [2] gives the expression

$$\frac{dN_R}{dt} = -\alpha_{max}\phi_0 \frac{N_R}{N_T} \exp\left(-\alpha_{max} \frac{N_R}{N_T} x\right) + \frac{N_T - N_R}{\tau}. \quad [3]$$

Considering that the absorption occurs mainly at the grain surface, one can take $x = 0$. When the system is at equilibrium, $dN_R/N_T = 0$ and expression [3] takes the form

$$\frac{N_R}{N_T} = \frac{1}{1 + \phi_0 \sigma \tau}. \quad [4]$$

Saturation occurs when N_R/N_T is significantly smaller than 1; this implies then that $\phi_0 \sigma \tau$ is large.

Therefore, for a given photon flux, saturation is favored for large absorption cross section σ and a long ^{1}E radiative lifetime τ. This theory, although oversimplified to describe in detail the behavior of such a complex system, confirms what could easily be expected: saturation occurs when the lifetime of the ^{1}E storage state is long, and when the cross section of the absorption transition is large. We have measured the ^{1}E radiative lifetime τ for $Ba_{10}(PO_4)_6F_2$:Mn 0.1% to be $\tau = 742$ μs at 77 K. This lifetime is rather long because of the spin forbidden character of the $^1E \rightarrow {}^3A_2$ transition, thereby favoring saturation effects.

We have seen that saturation occurs only for the $^3A_2 \rightarrow {}^3T_1(^3F)$ and charge transfer bands which are spin and symmetry allowed. This is consistent with theory and confirms the assignments of the 315- and 405-nm absorption bands to a charge transfer transition (large σ value) and to the $^3A_2 \rightarrow {}^3T_1(^3P)$ forbidden transition (low σ value), respectively. The relative intensity change of the 405 nm and visible absorption bands due to saturation effects is responsible for the color modification of the Mn-doped apatites when x increases. Charge transfer transitions are not involved in this phenomenon.

4.3. Influence of the B(V) Cation Site Size on the Coloration of Mn(V)-Doped Apatites

In order to study the influence of *B*(V) cation site size on the Mn(V)-doped apatites coloration, the barium phosphate apatite has been compared with the barium vanadate apatite. As the V–O mean bond length is 1.71 Å (36), while the P–O bond length is 1.54 Å (18), a variation of the crystal field strength experienced by the Mn(V) from one matrix to the other could be expected.

Figure 9 presents the diffuse reflectance spectra of Mn(V) in the two matrices. Notice that the spectra of Mn(V) in the phosphate and vanadate compounds are identical, excepted for the UV range beyond 315 nm, where charge transfer transitions associated with the vanadate group occur. This unexpected invariability of the crystal field experienced by Mn(V) can be understood considering the results of structural investigation of the Mn(V) local environment. This study was performed using X-ray diffraction (32), EXAFS, and vibrational spectroscopy (37, 38). The main result obtained is that in all Mn(V)-substituted barium vanadate or phosphate apatites, the Mn–O bond length is equal to 1.72 ± 0.02 Å independent of the Mn(V) content, x. It is concluded that the $(MnO_4)^{3-}$ ion imposes its own size to the host lattice and not the reverse. This explains why the crystal field strength remains constant.

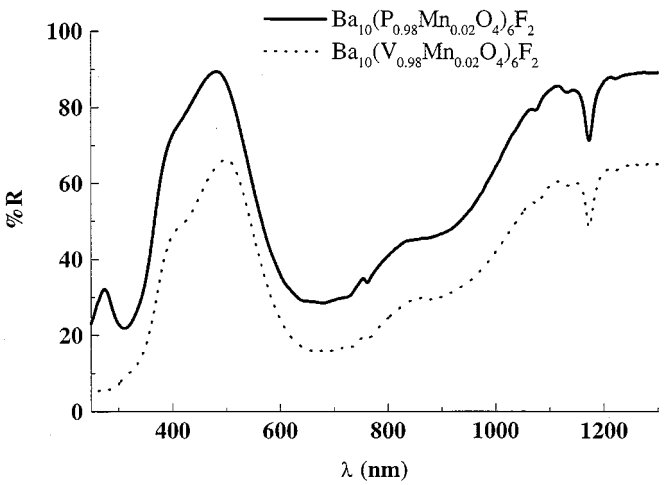

FIG. 9. Diffuse reflectance spectra of $Ba_{10}(P_{0.98}Mn_{0.02}O_4)_6F_2$ (solid line) and $Ba_{10}(V_{0.98}Mn_{0.02}O_4)_6F_2$ (dotted line).

It has already been mentioned in the literature that the $(MnO_4)^{3-}$ anion does not necessarily adopt the host site geometry in other Mn(V)-doped compounds with apatite and spodiosite structure (1, 10, 15, 19). The present work gives further examples of this absence of any matrix effect. However, in several cases, very sensitive methods such as EPR (1, 10, 15, 19) have revealed that $(MnO_4)^{3-}$ ions do experience some distortions, which varies from one host to another, even within the same structural family.

4.4. Influence of the A Cation on the Color of Mn(V)-Doped Apatites

We have investigated the effect of the nature of the alkaline-earth ion on the Mn(V) diffuse reflectance spectra for the phosphates and vanadates fluoroapatites. It has been shown previously that the diffuse reflectance spectra of manganese substituted barium phosphate and vanadate apatites are identical. The behavior of the vanadate or phosphate apatite as a function of the nature of the A cation are similar. Thus, we will discuss only the case of the phosphate apatites $A_{10}(PO_4)_6F_2$ (A = Ca, Sr, Ba) with a manganese content of 1%.

The diffuse reflectance spectra are given in Fig. 10. It can be seen that the diffuse reflectance bands shift toward longer wavelengths across the series A = Ca, Sr to Ba. This phenomenon has already been observed by Grisafe *et al.* for similar compounds (10% Mn doped mixed (Sr, Ba) phosphates or vanadates chloroapatites) (2). However, these authors did not interpret the shift of absorption bands.

Both the bands corresponding to the spin allowed transition to the $^3T_1$ and $^3T_2$ states and the zero-phonon lines associated with the transitions between the ground state and the ^1E and $^1A_1$ states are shifted. A variation of the crystal field parameter Dq is expected to shift the spin allowed transition bands, but not the zero-phonon lines. Indeed, the ^1E and $^1A_1$ energy state curves are parallel to the $^3A_2$ (Dq/B axis) in the Tanabe–Sugano diagram (39) of tetrahedral d^2 ions, which means that the $^3A_2 \rightarrow {}^1E$ and $^3A_2 \rightarrow {}^1A_1$ transitions energies are independent of the crystal field strength. This arises from the fact that the $^3A_2$, ^1E, and $^1A_1$ states belong to the same e^2 electron configuration (Fig. 3). The displacement of the bands must result, at least partially, from a Racah B and C parameters variation, reflecting a change in the Mn–O bond covalency. This can be confirmed by considering the relative displacement of the ^1E and $^1A_1$ (Δ^1E and Δ^1A_1) lines observed. For instance, $\Delta^1E = 117\ cm^{-1}$, $\Delta^1A_1 = 285\ cm^{-1}$ for shifts in barium and strontium apatites spectra. The ratio of these displacements, $\Delta^1E/\Delta^1A_1 = 0.41$, is in good agreement with the theoretical value to first order of 0.5 (39).

The shift of the spectra depicted Fig. 10 indicates that B and C Racah parameters decrease in the series Ca > Sr > Ba. Since a reduction of these electronic repulsion parameters implies an increase of the bond covalenced (39), the Mn–O bond covalency must increase in the series Ca < Sr < Ba. This corresponds to a decrease in the electronegativity of the alkaline-earth cations as well as their polarizing ability from Ca to Ba. Therefore, the electron density around the oxygen ions of the A coordination polyhedra must increase from Ca to Ba. Since, as already pointed out in the X-Ray diffraction study section, these oxygen ions are only linked to B (Mn) cations, the Mn–O bond covalency increases in the same order.

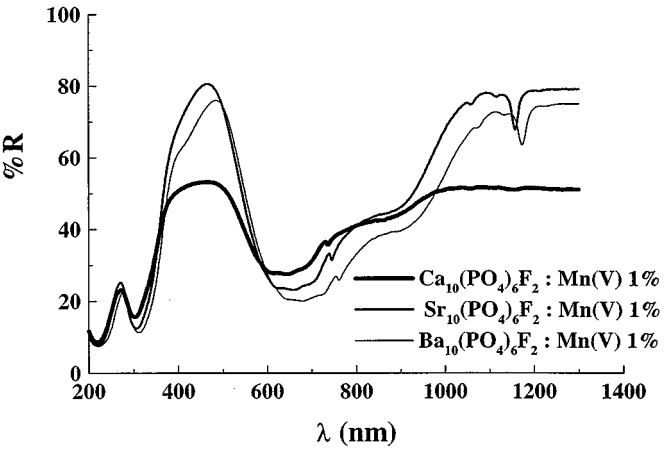

FIG. 10. Diffuse reflectance spectra of 1% manganese subtituted apatites $A_{10}(PO_4)_6F_2$ A = Ca, Sr, Ba.

5. CONCLUSION

The substitution of manganese (V) at B sites in fluoroapatites $A_{10}(BO_4)_6F_2$ (A = Ca, Sr, Ba and B = V, P) gives rise to bright turquoise blue to green coloration. The study of Mn(V) optical absorption changes in a substitution series using diffuse reflectance spectroscopy reveals two origins for this color change.

— The first, arising from the increase of the manganese content, is related to a selective saturation of the optical transitions with high absorption cross sections. Indeed the modification of the relative intensities of the absorption bands in the visible range generated by this saturation phenomenon explains the color change.

— The second cause is Mn–O bond covalency variation induced by the changing of the A–O bond ionicity. The increasing covalency of the Mn–O bond from Ca to Ba apatite leads to a reduction of the B and C Racah parameter and consequently to a shift of the absorption bands to longer wavelength.

In contrast, the diffuse reflectance spectra of homologous phosphate or vanadate apatites having the same Mn(V) content are identical. For all the compounds studied, the color changes are not apparently associated with crystal

field effects. Indeed, the crystal field strength experienced by the tetrahedral Mn(V) ions remains constant. This is confirmed by structural investigations (32, 37, 38), which combined with the present results, show that the Mn(V)-substituting ion retains its own size in the host lattice, instead of adopting the environment of the ion it replaces in the host lattice, as is often assumed.

REFERENCES

1. H. Lachwa and D. Reinen *Inorg. Chem.* **28,** 1044 (1989).
2. D. A. Grisafe and F. A. Hummel *J. Solid State Chem* **2,** 167 (1970).
3. T. Brunold, M. Herren, U. Oetliker, H. U. Güdel, U. Kesper, C. Albrecht, and D. Reinen, *J. Lumin.* **60/61,** 138 (1994).
4. U. Oetliker, M. Herren, H. Güdel, U. Kesper, C. Albrecht, and D. Reinen, *J. Chem, Phys.* **100,** 8656 (1994).
5. H. R. Verdun, "OSA Proceedings on Advanced Solid-State Lasers," Vol. **15,** p. 315 (1993).
6. T. C. Brunold, A. Hauser, and H. U. Güdel, *J. Lumin.* **59,** 321 (1994).
7. T. C. Bruold, H. U. Güdel, S. Kück, and G. Huber, *J. Lumin.* **65,** 293 (1996).
8. S. Kück, K. Petermann, U. Pohlmann, and G. Huber, *Phys. Rev. B* **51,** 17323 (1995).
9. L. D. Merkle, T. H. Allik, and B. H. T. Chai, *Opt. Mater.* **1,** 91 (1992).
10. C. Albrecht, S. Cohen, I. Mayer, and D. Reinen, *J. Solid State Chem.* **107,** 218 (1993).
11. J. A. Capobianco, G. Cormier, R. Moncorgé, H. Manaa, and M. Bettineli, *Appl. Phys. Lett.* **60,** 163 (1992).
12. J. A. Capobianco, G. Cormier, C. A. Morrison, and R. Moncorgé, *Opt. Mater.* **1,** 209, (1992).
13. M. Herren, H. U. Güdel, C. Albrecht, and D. Reinen, *Chem. Phys. Lett.* **183,** 98 (1991).
14. J. A. Capobianco, G. Cormier, M. Bettinelli, R. Moncorgé, and H. Manaa, *J. Lumin.* **54,** 1 (1992).
15. D. Reinen, W. Rauw, U. Kesper, M. Atanasov, H.U. Güdel, M. Hazenkamp, and U. Oetliker, *J. Alloys Compounds* **246,** 193 (1997).
16. N. Faure, Univ. thesis, Grenoble, France, 1992.
17. D. A. Grisafe and F. A. Hummel, *J. Solid State Chem.* **2,** 160 (1970).
18. M. Mathew, I. Mayer, B. Dickens, and L. W. Schroeder, *J. Solid State Chem.* **28,** 79 (1979).
19. D. Reinen, H. Lachwa, and R. Allmann, *Z. Anorg. Allg. Chem.* **542,** 71 (1986).
20. M. Evain, "U-Fit Software: A Cell Parameters Refinement Program." IMN, Nantes, France, 1992.
21. H. M. Rietveld, *J. Appl. Crystallogr.* **2,** 65 (1969).
22. J. Rodriguez-Carvajal, in collected abstract of powder diffraction meeting, Toulouse, Vol. 127 (1990).
23. A. E. Lavat, S. B. Etcheverry, and E. J. Baran, *Z. Naturforsch.* **41b,** 987 (1986).
24. S. G. Manca and E. J. Baran, *Anal. Assoc. Quim. Argentina* **70,** 583 (1982).
25. R. D. Shannon, *Acta Crystallogr., Sect. A* **32,** 751 (1976).
26. A. R. West, "Solid State Chemistry and its applications," Chap. 10. Wiley, New York, 1984.
27. Gustav Kortüm, "Reflectance Spectroscopy: Principles, Methods, Applications." Springer-Verlag, Berlin/New York, 1969.
28. M. A. Scott, B. Henderson, H. G. Gallagher, and T.P.J. Han, *J. Phys.: Condens, Matter* **9,** 9893 (1997).
29. M. Atanasov, H. Adamsky, and D. Reinen, *Chem. Phys.* **202,** 155 (1996).
30. U. Oetliker, M. Herren, H. Güdel, U. Kesper, C. Albrecht, and D. Reinen, *J. Chem. Phys.* **100,** 8656 (1994).
31. M. A. Scott, D. L. Russell, B. Henderson, T. P. J. Han, H. G. Gallagher, *J. Crystal Growth* **183,** 366 (1998).
32. K. Dardenne, Univ. thesis, Paris VI, France, October 28, 1998.
33. G. Blasse and B.C. Grabmaier, *in* "Luminescent Materials," p. 114. Springer-Verlag, Berlin Heidelberg, 1994.
34. T. C. Brunold and H. U. Güdel, *Chem. Phys. Lett.* **249,** 77 (1996).
35. H. Lachwa and D. Reinen, *Inorg. Chem.* **28,** 1044, (1989).
36. D. L. Corker, *Acta Crystallgr., Sect. C* **51,** 549 (1995).
37. K. Dardenne, D. Vivien, F. Ribot, G. Chottard, and D. Huguenin, *Eur. J. Solid State Inorg. Chem.* **35,** 419 (1998).
38. K. Dardenne, D. Vivien, F. Ribot, A. Kahn-Harari, and D. Huguenin, to be published.
39. A. B. P. Lever, "Inorganic Electronic Spectroscopy," Second ed., Elsevier, Amsterdam, 1984.